

Abstract

Eruptions at shield volcanoes often occur from radially aligned linear fissures fed by blade-like magma-filled cracks (dykes). The fissures of the 2018 Sierra Negra eruption were scattered on the flank of the volcano. Space-borne radar interferometric data (InSAR) revealed that, unexpectedly, part of the eruption was fed by a 15 km long, tortuous and flat-lying crack (sill). Here we develop a framework that captures the full 3D kinematics of non-planar intrusions. This includes both an analytical and comprehensive numerical scheme. We constrain the models such that they match the observed ground deformation at Sierra Negra. We show that the peculiar sill trajectory is due to the competing stress gradient magnitudes being close to one another throughout its propagation. By accounting for the interaction of all these factors, these 3D models open the possibility to understand and simulate the geometry of magma transport at volcanic systems.

Plain Language Summary

Here, we show in unprecedented detail using space-borne radar interferometric data, a large volume eruption at Sierra Negra volcano, Galápagos Islands fed by a flat-lying crack (sill). The observations are particularly intriguing as this sill's trajectory was over 15-km-long and whilst it remained flat it was highly curved, which, cannot be explained by existing models. We employ simple fracture mechanics models to show that the sill grew away from the summit due to the stresses induced by the slope of the volcano. Further from the summit, forces caused by the magma/rock weight contrast began to compete with the slope stresses causing the sill's growth direction to turn as observed. We show how parameters such as: magma volume, weight contrast, sill depth and the tectonic stresses, play a role in defining if/where the flank eruption occurs. To summarise, we show a well constrained example of a curved sill-fed eruption, which has never been observed in such detail before. These observations warranted the use of new 3D models to help explain the process. This work shows how to analyse the paths of cracks feeding volcanic flank eruptions efficiently in 3D, and can be used to understand the potential hazard of a particular batch of magma.

1 Introduction

Dyking is a form of magma transport through cracks driven by the pressure of the magma. Current dyke propagation models are two-dimensional (2D), taking advantage of the observed sheet-like aspect ratios of such fractures (Dahm, 2000; Sigmundsson et al., 2015; Pinel et al., 2017). 2D models capture the processes driving many dykes, but cannot be used to explain observations of dykes twisting or segmenting, and dyke ascent followed by lateral propagation (Bagnardi et al., 2013; Xu & Jónsson, 2014; Sigmundsson et al., 2015). One striking example of more complex propagation is the intrusion feeding the 2018 Sierra Negra eruption. Surface deformation patterns revealed by space-borne radar interferometric data (InSAR) data show a surprising geometry and trajectory of the propagating feeder. The deformation patterns point at a flat-lying magma body (sill) with a propagation direction that turned by over 90 degrees, whilst the sill remained flat-lying. Magma rarely propagates for long distances as a sill. Observations from previous eruptions at the Galápagos islands show many such sills twisting into dykes before they erupt (Bagnardi et al., 2013). Rare examples of sill propagation include the May 2016 eruption at Piton de la Fournaise, La Réunion (Smittarello et al., 2019) and the intrusions tracked by the 2011-2013 El Hierro seismic swarms (Cerdeña et al., 2018; González et al., 2013). Comprehensive, three-dimensional (3D) propagation models to understand the tortuous path of such sills and dykes are not available.

Here we combine current 2D fluid-filled fracture mechanics models with the advancements from other fields in the 3D growth of fractures (Meng et al., 2013; Nejati et al.,

69 2016). After evaluating ground displacement observations of the 2018 Sierra Negra in-
70 trusion, we use the new models to explain the curved propagation path of the sill.

71 2 Observations and data

72 Sierra Negra is an intra-plate basaltic shield volcano with a maximum elevation of
73 1140 metres above sea level (m.a.s.l.), a shallow (110 m) and structurally complex 7 x
74 10 km elliptical caldera, and is the most voluminous of the five coalescing volcanoes that
75 form Isabela Island in the western Galápagos Archipelago, Ecuador (Reynolds et al., 1995).
76 Thirteen effusive eruptions have occurred at Sierra Negra since 1813. The three most
77 recent eruptions all occurred in the northern flank of the volcano and emplaced 0.90 km^3
78 in 1979, 0.15 km^3 in 2005, and 0.19 km^3 of lava in 2018 (Vasconez et al., 2018). The 1979
79 and 2005 eruptions were fed by vents high on the northern flank and with eruptive fis-
80 sures aligned parallel to the caldera rim and were likely fed by circumferential dykes (e.g.,
81 (Geist et al., 2008)). In contrast, the vents of the 2018 eruption were scattered with no
82 preferred orientation up to 9.5 km from the caldera rim, at a minimum elevation of 90
83 m.a.s.l. There are no documented examples of vents at such low elevations in the recent
84 history of the volcano. On the other hand, some of the higher-elevation eruptive vents
85 of the 2018 eruption reactivated existing fissures. The 2018 eruption interrupted a thirteen-
86 year semi-continuous period of uplift that raised the floor of the summit caldera by up
87 to 5.2 m since the 2005 eruption as measured by GPS (Fig. S1), presumed to be re-pressurization
88 of a ~ 2 km deep magma reservoir.

89 On the 26th June 2018 at 19.40 UTC the appearance of volcanic tremor marked
90 the beginning of the eruption. Throughout the eruption, seismicity was mainly located
91 along the caldera fault system with fewer events in the northwestern upper flank. Caldera
92 deflation rapidly started with the onset of eruptive activity and by the time the erup-
93 tion ended on the 25th August 2018, GPS stations measured a cumulative intra-caldera
94 subsidence of up to ~ 8.5 m (Fig. S1).

95 Short-lived (< 24 hrs) effusive eruptions from multiple fissures (Fissure 1 - 5, Fig. 1)
96 on 26-27 June were followed by a long-lasting effusive eruption from the most distal fis-
97 sure (Fissure 6) between July 1st and August 25th. Geodetic monitoring by continuous
98 GPS at Sierra Negra is limited to the summit caldera, such that the feeder-induced sur-
99 face displacements were only measured by interferometric synthetic aperture radar (In-
100 SAR). The first co-eruptive synthetic aperture radar (SAR) image was acquired on 29
101 June at 17:50 UTC by the Japan Aerospace Exploration Agency's ALOS-2 satellite, ap-
102 proximately 70 hours after the onset of the seismic swarm (Fig. 1). Further SAR images
103 were acquired on 30 June and 1 July by the European Space Agency's Sentinel-1 satel-
104 lite constellation, right before the opening of Fissure 6 (Fig. 2a and b). Additional SAR
105 images were captured during the eruption of Fissure 6 (Fig. 2c and d). Surface defor-
106 mation patterns before and after Fissure 6 erupted show the trajectory for the propa-
107 gating feeder (Table. S1). We estimate the location and geometry of the source of de-
108 formation using a Bayesian approach (see Fig. S2 and Table. S1 for a description of the
109 methodology and results).

110 3 Model

111 Here we outline the basic principles used in our method. After this introduction,
112 we tackle the problem both analytically and with numerical simulations.

113 Propagation directions of dykes have typically been predicted by maximizing the
114 strain energy release rate (Dahm, 2000; Sigmundsson et al., 2015), on test elongations
115 at the leading tip, thereby finding the path of least resistance. Such a method is unwieldy
116 for true 3D propagation, as it would involve computing a large number of potential tip-

Figure 1. a) Inset map showing the location of Sierra Negra volcano. Volcanoes labelled as Wolf (W), Darwin (D), Fernandina (F), Alcedo (A), Sierra Negra (S) and Cerro Azul (C). b) Interferogram spanning the sill propagation phase of the 2018 eruption. SAR data from the ALOS-2 satellite. Each colour cycle represents 11.45 cm displacement, positive towards the satellite (e.g. uplift) and negative away from it (e.g. subsidence). Gray polygons show the extent of the lava flows emplaced during the time period spanned by the interferogram. Yellow lines mark the location and extent of all eruptive fissures. Black triangles mark the location of GPS stations. Black arrows show the satellite orbit direction (\sim N-S), look direction (\sim E-W), and the incidence angle in degrees. Descending pass, Track 147, ScanSAR mode.

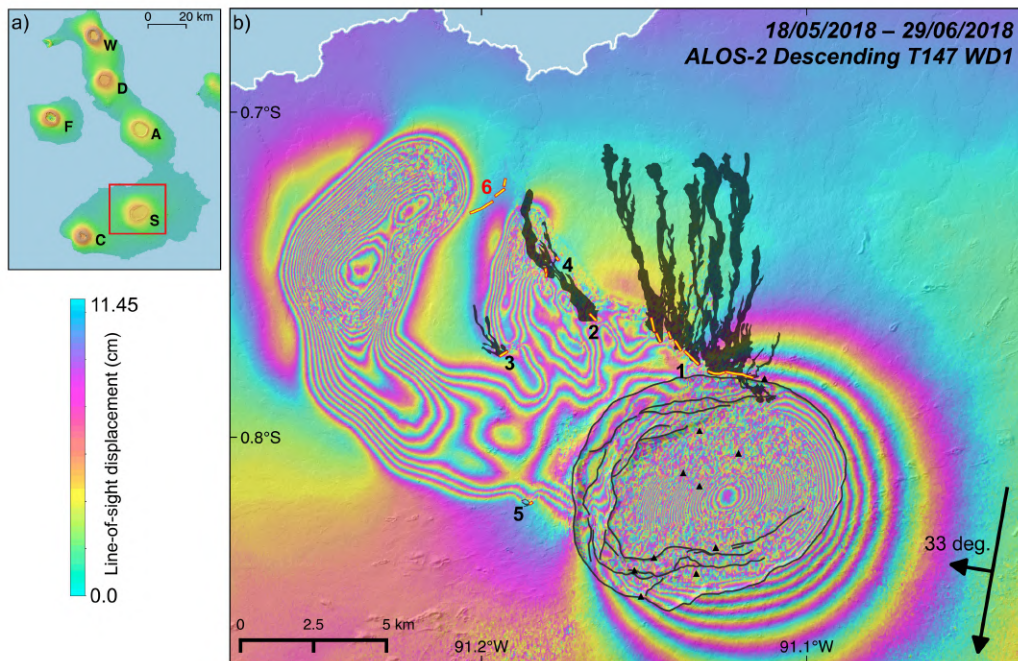
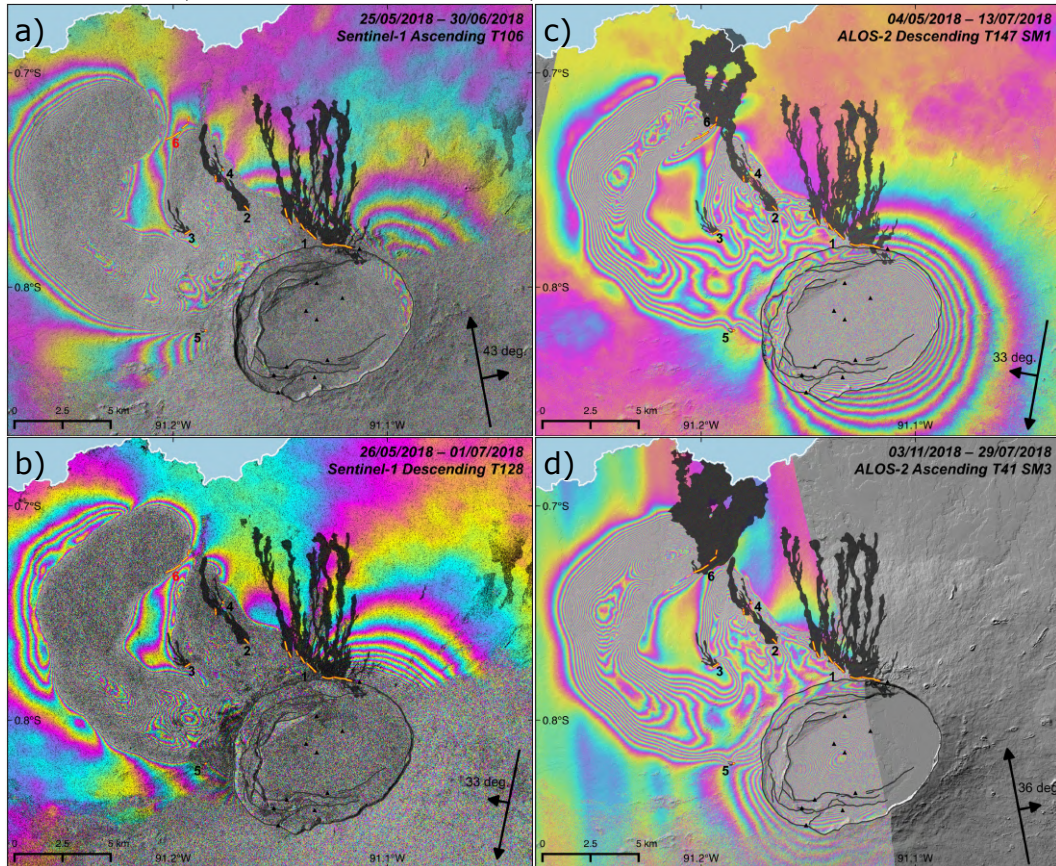


Figure 2. Interferograms of Sierra Negra spanning the sill propagation and eruption phase of the 2018 eruption. SAR data are from the Sentinel-1 satellite (a and b) and the ALOS-2 satellite (c and d). Same colourbar as Fig. 1, with each colour cycle in (a and b) as 2.8 cm and in (c and d) 11.45 cm displacement, positive towards the satellite (e.g. uplift) and negative away from it (e.g. subsidence). Black arrows show the satellite orbit direction, a) ~ S-N b) ~ N-S, look direction a) ~ W-E b) ~ E-W, and the incidence angle in degrees. a) Ascending pass, Track 106, TOPS mode. b) Descending pass, Track 128, TOPS mode. c) Descending pass, Track 147, Ultra-fine Stripmap mode (SM1; pixel resolution 3.0x3.0 m). d) Ascending pass, Track 41, Fine Stripmap mode (SM3; pixel resolution 9.1x5.3 m). Symbols as in Fig. 1.



117 line growth patterns. Here we use a theoretically equivalent, but more flexible, approach
118 based on the maximum stress intensity, K .

119 In our analytical approach, we reduce the sill geometry to that of a penny-shaped
120 crack subject to stress gradients, with an opening that is compatible with the surface
121 displacements observed along the short-axis of the sill. At selected points along the sill's
122 path, we calculate K around the tip-line (Davis et al., 2019), and assume the greatest
123 tip-line advance occurs in the direction where K is largest (akin to Paris fatigue law (Davis
124 et al., 2020)). In our numerical simulations, we discretise the sill into triangular elements
125 (Nikkhoo & Walter, 2015; Davis et al., 2020) and update the tip-line at each step using
126 the local value of K as compared to the critical rock strength, K_c . The total stress in-
127 tensity which is compared to the fracture toughness at a point of a crack's tip-line can
128 be defined by a combination of the opening, sliding and tearing mode stress intensity fac-
129 tors (Pollard & Fletcher, 2005) (K_I , K_{II} and K_{III}).

$$K = \sqrt{K_I^2 + K_{II}^2 + \left(\frac{1}{1-\nu}\right) K_{III}^2} \quad (1)$$

130 which relates to strain energy release rate (Tada et al., 2000) (\mathcal{G}) through:

$$K = \sqrt{\frac{\mathcal{G}E}{1-\nu^2}}; \quad (2)$$

131 where E is Young's modulus.

132 In our analytical approach, we employ stress intensity equations in a full-space. We
133 then go on to numerically test how the free surface and the real topography would af-
134 fect these results. In the numerical simulations, we compute stresses under an arbitrary
135 topography in 3D with an external elastic stress field. As in previous 3D studies we ne-
136 glect viscous effects of the contained fluid and coupling to a depressurizing chamber.

137 We constrain the parameters in both models using inversions of co-eruptive InSAR
138 data along the propagation path (Fig. S2, Table. S1): depth $d=950$ m, radius $c=1900$
139 m and volume $V=1.6\pi c^2$ m³. V represents the volume of the inflated nose of the prop-
140 agating fracture, which is approximately a tenth of the estimated erupted volume (Vasconez
141 et al., 2018) (0.018 km³). We set the rock properties to: $\rho_r=2900$ kg·m⁻³, $\mu=2\cdot 10^9$ Pa
142 and $\nu=0.35$ corresponding to the rock density, shear modulus and Poisson's ratio, re-
143 spectively. These properties lie towards the more compliant end of reported stiffness val-
144 ues from outcropping lava flows in Kilauea, Hawaii (Bubeck et al., 2017).

145 4 Effects defining the sill's path

146 We begin by reducing the physics of this problem into its component parts and eval-
147 uate how these affect the sill's direction of propagation. Previous studies have found that
148 dyke trajectories are dependent on the ratio of tectonic to topographic loading stresses
149 (Roman & Jaupart, 2014; Sigmundsson et al., 2015; Rivalta et al., 2019). Here we pro-
150 pose that contrasting magma and rock weight gradients (buoyancy) must also be con-
151 sidered as one of the dominant forces.

152 Opening stress intensity K_I around the edge of a penny-shaped crack of volume
153 V in a full-space, subject to a constant pressure (Tada et al., 2000) is:

$$K_I = \frac{3\mu V}{4(1-\nu)c^2\sqrt{\pi c}} \quad (3)$$

154 K_I around a crack under a pressure gradient (Tada et al., 2000) is:

$$K_{I\alpha} = \frac{4}{3\pi} \Delta\gamma c \sqrt{\pi c} \cos(\alpha) \quad (4)$$

155 where α is the angle away from the direction of the linear stress gradient ($\Delta\gamma$) on the
 156 crack's walls. The pressure gradient in equation 4 defines the direction of K_{max} (blue
 157 lines in Fig. 3a). As such, ignoring other effects, the direction and magnitudes of compet-
 158 ing pressure gradients acting on the crack define its propagation direction.

159 We now estimate stress gradients at Sierra Negra. First, we use an analytical solu-
 160 tion describing stresses beneath a symmetrical ridge-like topography (Savage et al., 1984) which
 161 we align at fit to the topographic profile between A-A' shown in Fig.3. This approximate
 162 topographic slope is shown in Fig.4c) and in the supplementary materials. h and v are
 163 the horizontal and vertical axis, respectively. We compute the horizontal gradient of ver-
 164 tical stress: $\delta\sigma_v/\delta h$, i.e., the normal stress gradient driving a flat-lying crack away from
 165 the caldera rim, at the inferred sill depth along its track. Linear stress gradients due to
 166 the difference between rock and fluid density (buoyancy) (Pollard & Townsend, 2018)
 167 are $(\rho_r - \rho_f)g \sin(\beta)$, where ρ_f is the magma density. The factor $\sin(\beta)$ means that if
 168 the crack is flat this gradient is zero. We set $\rho_f = \rho_r - 300 \text{ kg}\cdot\text{m}^{-3}$ (Vigouroux et al.,
 169 2008). For the parameters above, 15 km from the caldera center (around where the sill
 170 began to turn eastwards) the dip needs to be around 10° for the buoyancy gradient to
 171 exceed the stress gradient due to the overlying slope (Fig. S3) and drive the sill to turn
 172 away from the downslope direction (Fig. 3a).

173 It is well-documented that sills curve upwards, towards a free surface (Thomas &
 174 Pollard, 1993). We find, for a penny-shaped crack, where $c/d=2$, as observed, a dip of
 175 15° results in the same K_I increase for both buoyancy and the free surface, doubling dip's
 176 effects (see supplementary material S4).

177 Lastly, we test if the other intrusions to the east that fed fissures 2, 3 and 4 (Fig. 1)
 178 may have attracted the sill. Two penny-shaped cracks subject to equal internal pressure
 179 separated 5 km from each other, as observed (tip separation of 1.2 km) experience a max-
 180 imal K_I increase of $\sim 3\%$ (Tada et al., 2000; Fabrikant, 1987). Such an increase is mi-
 181 nor compared to the processes described earlier.

182 To summarise the analytical analysis, the stress gradient due to topography drives
 183 the sill away from the caldera rim. As the slope shallows, the buoyancy gradient begins
 184 to dominate even for shallowly dipping cracks, causing the sill to turn. The free surface
 185 amplifies this effect (Fig. S5). This analytical method of assessing the sill path is flex-
 186 ible and fast.

187 In order to allow interaction between all factors discussed above, we develop a 3D
 188 Boundary Element Model (Davis et al., 2019, 2020) to simulate a penny-shaped crack
 189 beneath the real edifice's topography. We include stresses due to gravitational loading
 190 and traction-free boundary conditions on the surface (Martel, 2000; Davis et al., 2019).
 191 Using orientations of the crack in the 3D space obtained by inverting surface deforma-
 192 tion, our model explains the turning of the sill for snapshots along its path (Fig. 3), show-
 193 ing that it is the interaction between sill dip, slope gradients and the free surface that
 194 causes the observed turning. Note that increasing the ratio of the horizontal to vertical
 195 stress (σ_h/σ_v) in the topographic loading model results in better fits.

196 5 Full 3D propagation model

197 Lastly, we run full 3D fracture propagation simulations (Davis et al., 2020). Here
 198 the crack is neither constrained to be planar nor circular in shape, only such that it main-
 199 tains a constant V . The tip-line shape is recalculated at every iteration moving it for-
 200 ward in proportion to K/K_c , at any triangle where $K/K_c > 1$. We remove triangular

Figure 3. Simulating the propagation direction of fracture at selected locations a) Analytical K_I diagram. Black circles represent the fracture, distance of the dashed gray line to the fracture edge represents K_I magnitude, where the blue line represents K_{max} direction. Topographic contours shown in orange. b) Numerical simulation of the propagation direction at Sierra Negra. Fractures have been scaled to a 1 km radius for visualisation, white dashed-line represents K_I magnitude as in a). Dip and strike directions shown, defined by inversions (Table. S1). For P7 a dip of 15° is used. Dashed grey outline is a contour of sill-induced deformation from Fig. 2c). Background $\sigma_h/\sigma_v=0.5$ in topographic loading model.

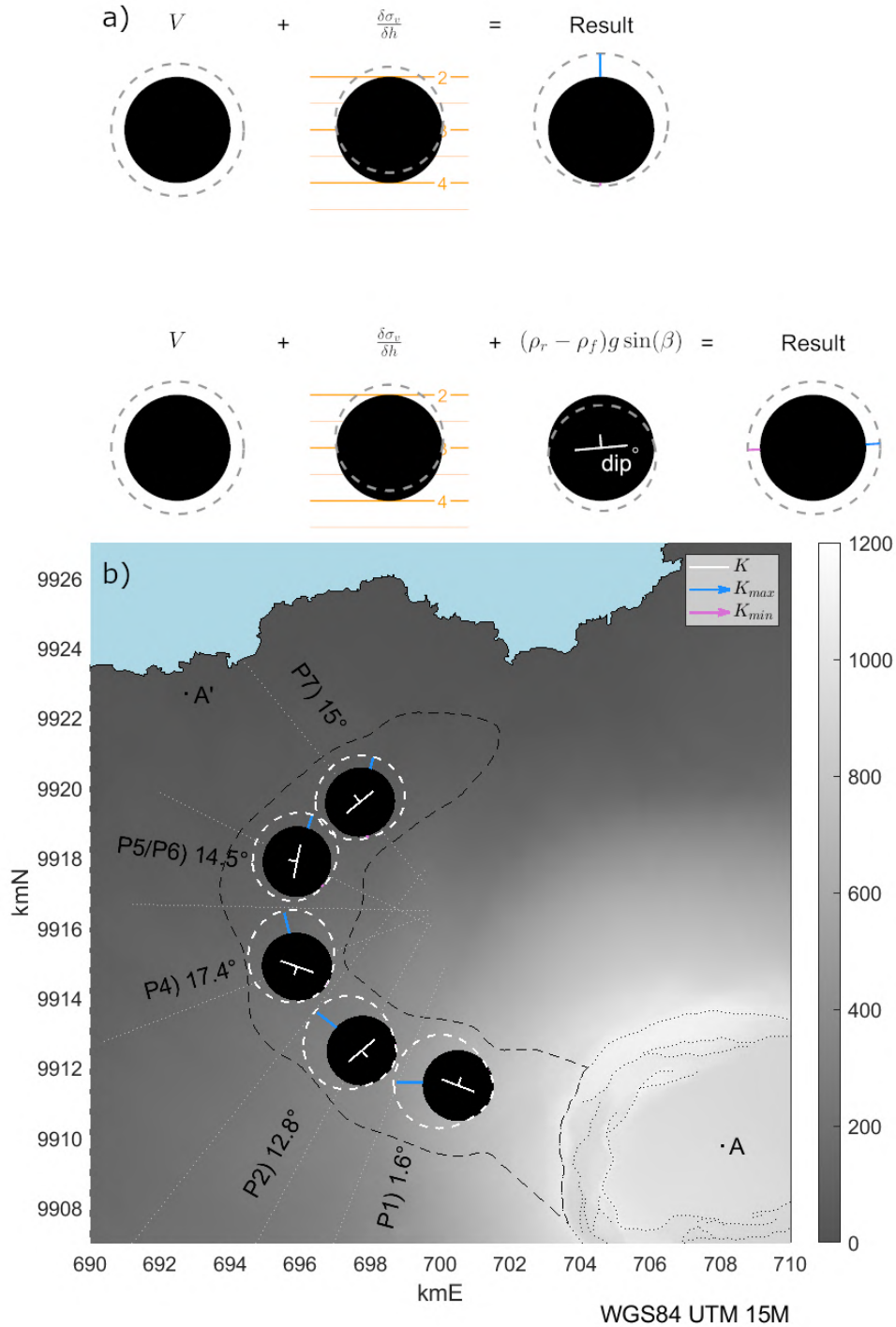
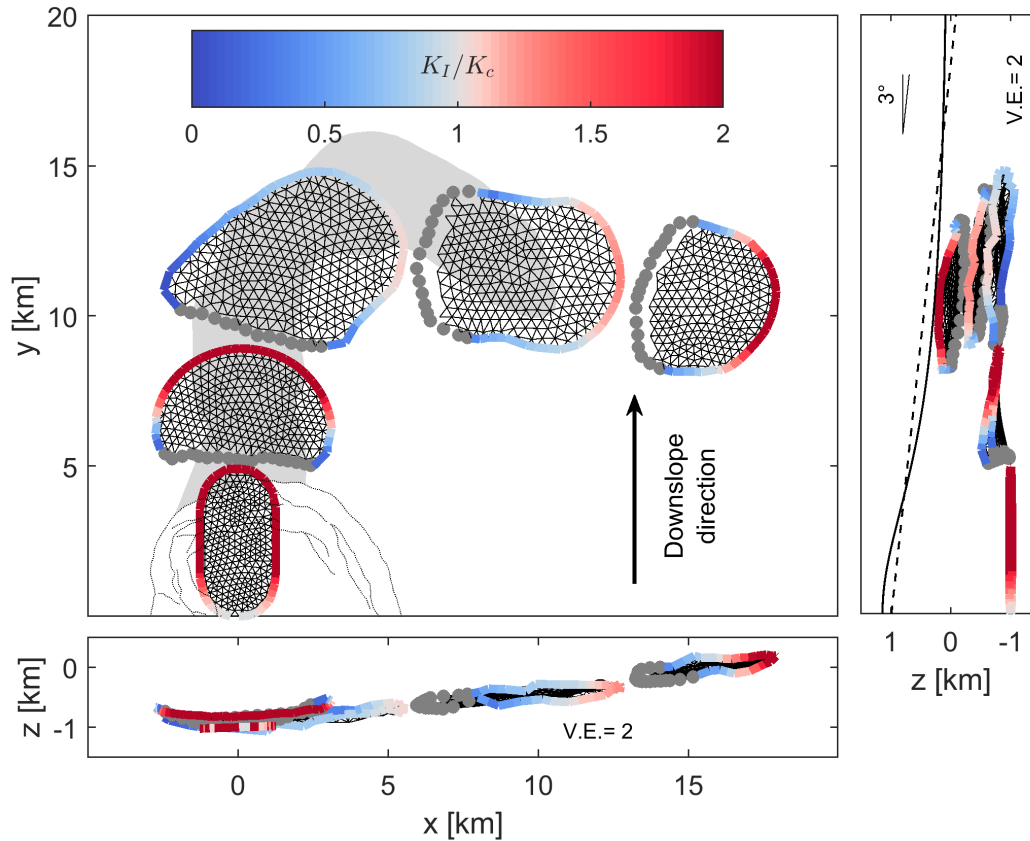


Figure 4. Numerical simulation of the sill propagation. a) Map view, b) cross-section looking along the downslope direction and c) cross-section looking along the x -axis with Vertical Exaggeration (V.E.). The fracture is shown at chosen locations along its computed path. Grey points are edges that closed in the previous iteration. The shaded patch in a) is the sill track and the dotted line is the caldera rim. In c) the solid line is the topographic slope used to load the body and the dashed line is the simulations free surface. Parameters used: $\beta = 1^\circ$, $\rho_f = \rho_r - 300$ kg/m³, start depth of 1000 m, $K_c = 70$ MPa \cdot m^{0.5}, $V = 1.6\pi c^2$ m³ and $\sigma_{yy} = -4.5$ MPa.



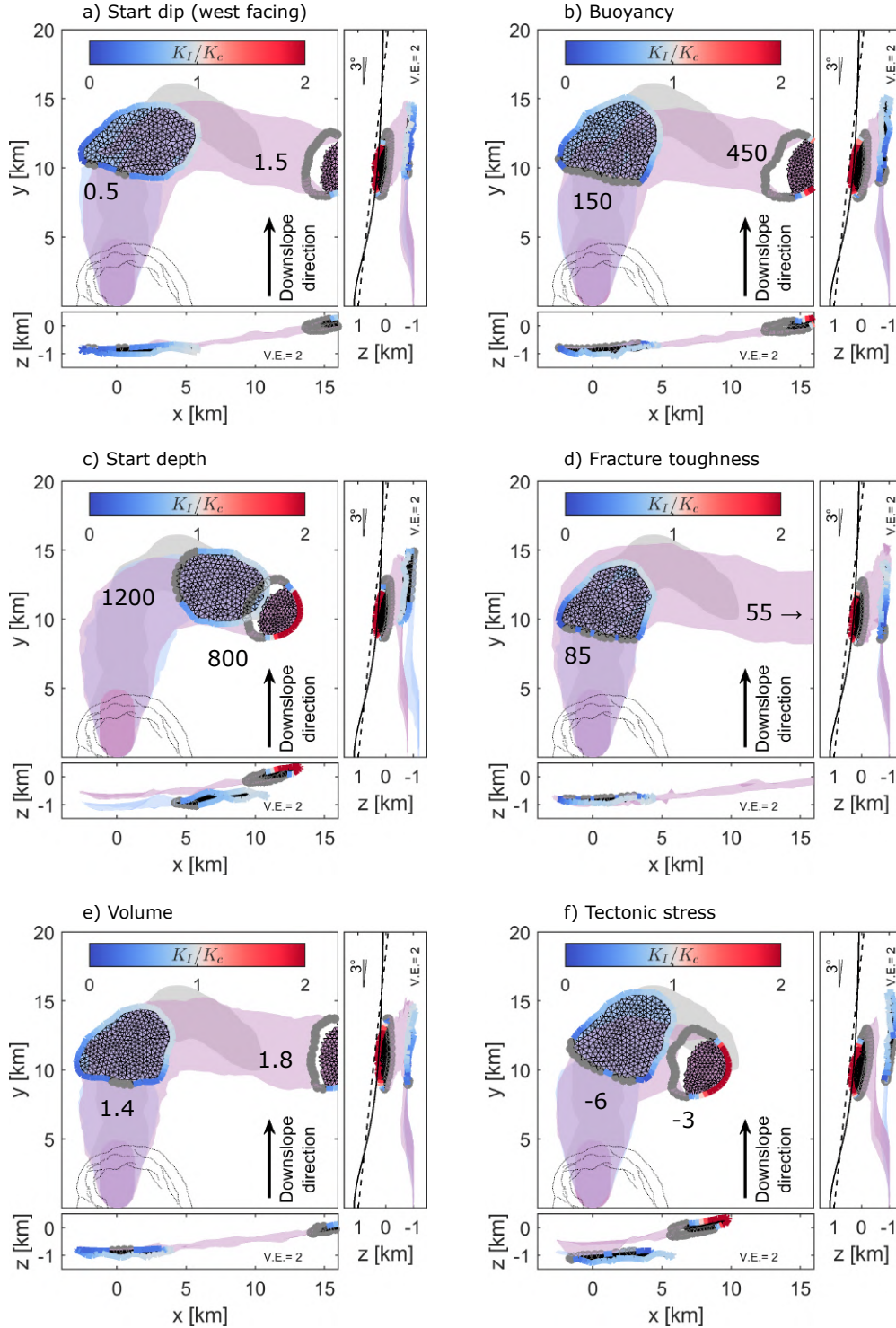
201 elements that shut closed. Bending or twisting of the fracture's tip-line out of its plane
 202 is calculated using the maximum circumferential stress criterion (Pollard & Fletcher, 2005).

203 In this last approach, we use a planar free surface with a start height at $y = 0$ of
 204 990 m with a slope of 3° facing to the north. The lithostatically stressed body ($\sigma_h =$
 205 σ_v) is loaded due to topography (Savage et al., 1984) (Fig. S3). We also apply through-
 206 out the body a compressive tectonic stress of 4.5 MPa directed along σ_{yy} , with σ_{xx} the
 207 mean between σ_{yy} and σ_{zz} , as suggested by stress indicators (Heidbach et al., 2018). Shear
 208 stresses from the topographic loading solution (Savage et al., 1984) are set to zero, on the
 209 assumption that these stresses are diminished over time by faulting, diking and longer
 210 term rock deformation processes in the edifice's flanks.

211 The initial crack is an ellipse 1000 m wide and 5000 m long at a depth of 1000 m
 212 below sea level, dipping to the west by $\beta=1^\circ$. K_c is set to 70 MPa \cdot m^{0.5}. We find when
 213 the fracture gets to a certain distance away from the caldera centre, it begins to turn and

214 propagates east (Fig. 4). By changing the values of the parameters one at a time, we in-
215 vestigate the sensitivity of the path to the input parameters and initial geometry (Fig. 5).
216 Reducing the initial start dip β or the buoyancy reduces the force driving the sill east-
217 wards, causing the sill to stall as the topography shallows (Fig. 5a/b). The start depth
218 defines when the free surface attraction takes effect (Fig. S5f), such that only shallower
219 sills can propagate eastwards (Fig. 5c). Flipping the start dip direction such that it is
220 west facing results in a mirror image of the path shown. The fracture toughness and vol-
221 ume define how far the sill can travel downslope as the topography shallows. These also
222 control the sill width, reducing the buoyancy force when this is smaller, again trapping
223 the sill (Fig. 5d/e). Increasing the material stiffness will have a similar effect to increas-
224 ing the fluid volume, see Eq. 3. When the tectonic compressive stress is reduced, in places
225 σ_v becomes the most compressive stress, causing the sills track to become very unsta-
226 ble with the sill quickly rising to the surface (Fig. 5f).

Figure 5. Effects of differing parameters on the simulated sill path, each sub-figure shows two simulations, from above and in cross section. In each sub-figure, one trajectory shown gets trapped and the other erupts. Fracture paths from the simulations are shown as coloured patches, where the blue is trapped and the pink erupts. The final mesh from each simulation, with the tip-line value of K is also shown, as in Fig. 4. In each simulation we changed one parameter with respect to Fig. 4, as follows: a) erupted: $\beta = 1.5^\circ$, trapped: $\beta = 0.5^\circ$. b) erupted: $\rho_f = \rho_r - 450 \text{ kg/m}^3$, trapped: $\rho_f = \rho_r - 150 \text{ kg/m}^3$. c) Start depth, erupted: 800 m, trapped: 1200 m. d) erupted: $K_c = 55 \text{ MPa} \cdot \text{m}^{0.5}$, trapped: $K_c = 85 \text{ MPa} \cdot \text{m}^{0.5}$. e) erupted: $V = 1.8\pi c^2 \text{ m}^3$, trapped $V = 1.4\pi c^2 \text{ m}^3$. f) erupted: $\sigma_{yy} = -3 \text{ MPa}$, trapped $\sigma_{yy} = -6 \text{ MPa}$. These parameters are also shown as text next to the final mesh of each simulation.



227 The simulations compare well with the observed trajectory; the sill was destined
228 to turn, although it could have stalled or erupted earlier on its path.

229 6 Discussion and conclusions

230 Firstly, we have developed a simple analytical model where we place a test-crack
231 at a point along the propagation path and evaluate how different stress gradients, rock
232 and magma parameters contribute to the propagation direction. This can be applied to
233 assess the dominant factors controlling an intrusion's path. For a given set of parame-
234 ters, using the equations above, one can also efficiently assess in which direction, and how
235 far, an intrusion can propagate. This may help in mitigating the risk linked to flank erup-
236 tions.

237 Secondly, we have outlined a numerical scheme where a dyke is discretised using
238 triangular, mixed-mode dislocations, allowing for simulation of non-planar and non-uniform
239 tip-line advance. For a given set of start parameters, this can simulate the entire prop-
240 agation geometry due to a given stress state and start volume. This can capture the full
241 3D growth and migration. This scheme is less time-efficient (in the order of hours for one
242 simulation) but is flexible and accounts for interacting processes.

243 It is of note that for this intrusion there are strong parameter trade-offs. By sim-
244 ulating the geometries of multiple observed flank eruption feeders, this scheme can be
245 used to retrieve better constraints on the state of edifice stresses, in particular the tec-
246 tonic directions and the ratio of horizontal to vertical stress (Rivalta et al., 2019).

247 Recent developments in hydrofracturing studies have shown how 3D fracture prop-
248 agation models that include fluid flow within the fracture are possible to implement, for
249 planar fractures (Salimzadeh et al., 2020; Zia & Lecampion, 2020). Such schemes could
250 be coupled to the model presented here to explain both the spatial and temporal evo-
251 lution of sills and dykes (Pinel et al., 2017; Zia & Lecampion, 2020; Salimzadeh et al.,
252 2020). It is of note that the simulation time increases rapidly when including this pro-
253 cess.

254 Previous flank volcanism at Galápagos volcanoes has been fed by radial and cir-
255 cumferential dykes (Chadwick Jr & Dieterich, 1995; Bagnardi et al., 2013). Here we have
256 shown evidence of flank volcanism fed by a long curving sill. We find that trajectories
257 of shallow sills underneath topography will be unstable and defined by a delicate bal-
258 ance between buoyancy forces, topographic load, external stresses and the free surface.
259 Still, trajectories may be anticipated, provided all those factors are well-constrained and
260 their interaction is accounted for, within three-dimensional dyke propagation models. By
261 combining such models with careful analysis of high-resolution crustal deformation data,
262 we showed that such parameters as well as the state of stress of the volcano can be well
263 constrained, reducing the uncertainties in the hazard.

264 Acknowledgments

265 T Davis is funded by the DFG-ICDP grant N. RI 2782/3-1. M. Bagnardi was supported
266 by an appointment to the NASA Postdoctoral Program at the Jet Propulsion Labora-
267 tory, administered by the Universities Space Research Association (USRA) through a
268 contract with NASA. Part of this research was carried out at the Jet Propulsion Lab-
269 oratory, California Institute of Technology, under a contract with the National Aeronau-
270 tics and Space Administration (grant 281945.02.47.04.51).

271 **Data availability statement:** InSAR data used in this manuscript are available
272 at <https://doi.org/10.5281/zenodo.4728054>. Sentinel-1 raw SAR data that support
273 the findings of this study are publicly available at <https://scihub.copernicus.eu/ALOS>

274 -2 raw SAR data availability is restricted to PI investigation at [www.eorc.jaxa.jp/ALOS/](http://www.eorc.jaxa.jp/ALOS/en/)
275 [en/](http://www.eorc.jaxa.jp/ALOS/en/).

276 **Code availability statement:** The code used for 3D boundary element numer-
277 ical analysis in this study was the open source Julia (Julia-1.5.0) code [https://doi.org/](https://doi.org/10.5281/zenodo.4726796)
278 [10.5281/zenodo.4726796](https://doi.org/10.5281/zenodo.4726796) and <https://doi.org/10.5281/zenodo.4727208> with an
279 interface (<https://doi.org/10.5281/zenodo.4727190>) with the Computational Ge-
280 ometry Algorithms Library (CGAL-4.13.1) software (C++) for meshing. The scripts used
281 in this analysis are uploaded in the repository: <https://doi.org/10.5281/zenodo.4727080>,
282 noting some of the MATLAB codes in this rely on functions from the author's open source
283 repository: <https://doi.org/10.5281/zenodo.3694164>.

284 **Author Contributions:** T.D and M.B coordinated the work and wrote the ini-
285 tial manuscript. M.B and P.L acquired and analysed the InSAR and GPS data in this
286 study. This analysis provided the evolution and geometry of the sill. T.D and E.R con-
287 ceptualised the analytical and numerical fracture mechanics that form the interpreta-
288 tion in this work. T.D wrote the analytical and numerical fracture mechanics codes used
289 in this study. All authors have read and revised the manuscript and contributed ideas
290 to the research.

291 References

- 292 Bagnardi, M., Amelung, F., & Poland, M. P. (2013). A new model for the growth of
293 basaltic shields based on deformation of fernandina volcano, galápagos islands.
294 *Earth and Planetary Science Letters*, *377*, 358–366.
- 295 Bagnardi, M., & Hooper, A. (2018). Inversion of surface deformation data for rapid
296 estimates of source parameters and uncertainties: A bayesian approach. *Geo-*
297 *chemistry, Geophysics, Geosystems*, *19*(7), 2194–2211.
- 298 Bubeck, A., Walker, R., Healy, D., Dobbs, M., & Holwell, D. (2017). Pore geom-
299 etry as a control on rock strength. *Earth and Planetary Science Letters*, *457*,
300 38–48.
- 301 Cerdeña, I. D., García-Cañada, L., Benito-Saz, M., del Fresno, C., Lamolda, H.,
302 de Pablo, J. P., & Sanz, C. S. (2018). On the relation between ground
303 surface deformation and seismicity during the 2012–2014 successive mag-
304 matic intrusions at el hierro island. *Tectonophysics*, *744*, 422–437. doi:
305 10.1016/j.tecto.2018.07.019
- 306 Chadwick Jr, W., & Dieterich, J. (1995). Mechanical modeling of circumferential
307 and radial dike intrusion on galapagos volcanoes. *Journal of Volcanology and*
308 *Geothermal Research*, *66*(1-4), 37–52.
- 309 Chen, C. W., & Zebker, H. A. (2001). Two-dimensional phase unwrapping with
310 use of statistical models for cost functions in nonlinear optimization. *JOSA A*,
311 *18*(2), 338–351.
- 312 Dahm, T. (2000). Numerical simulations of the propagation path and the arrest
313 of fluid-filled fractures in the earth. *Geophysical Journal International*, *141*(3),
314 623–638.
- 315 Davis, T., Healy, D., & Rivalta, E. (2019). Slip on wavy frictional faults: Is the 3rd
316 dimension a sticking point? *Journal of Structural Geology*, *119*, 33–49. doi: 10
317 .1016/j.jsg.2018.11.009
- 318 Davis, T., Rivalta, E., & Dahm, T. (2020). Critical fluid injection volumes for un-
319 controlled fracture ascent. *Geophysical Research Letters*, e2020GL087774.
- 320 Decriem, J., Árnadóttir, T., Hooper, A., Geirsson, H., Sigmundsson, F., Keiding,
321 M., ... others (2010). The 2008 may 29 earthquake doublet in sw iceland.
322 *Geophysical Journal International*, *181*(2), 1128–1146.
- 323 Fabrikant, V. (1987). Close interaction of coplanar circular cracks in an elastic
324 medium. *Acta Mechanica*, *67*(1-4), 39–59.
- 325 Geist, D. J., Harpp, K. S., Naumann, T. R., Poland, M., Chadwick, W. W.,

- 326 Hall, M., & Rader, E. (2008). The 2005 eruption of sierra negra vol-
327 cano, galápagos, ecuador. *Bulletin of Volcanology*, *70*(6), 655–673. doi:
328 10.1007/s00445-007-0160-3
- 329 González, P. J., Samsonov, S. V., Pepe, S., Tiampo, K. F., Tizzani, P., Casu, F., ...
330 Sansosti, E. (2013). Magma storage and migration associated with the 2011–
331 2012 el hierro eruption: Implications for crustal magmatic systems at oceanic
332 island volcanoes. *Journal of Geophysical Research: Solid Earth*, *118*(8), 4361–
333 4377. doi: 10.1002/jgrb.50289
- 334 Heidbach, O., Rajabi, M., Cui, X., Fuchs, K., Müller, B., Reinecker, J., ... others
335 (2018). The world stress map database release 2016: Crustal stress pattern
336 across scales. *Tectonophysics*, *744*, 484–498.
- 337 Martel, S. J. (2000). Modeling elastic stresses in long ridges with the displacement
338 discontinuity method. *Pure and Applied Geophysics*, *157*(6-8), 1039–1057.
- 339 Meng, C., Maerten, F., & Pollard, D. D. (2013). Modeling mixed-mode fracture
340 propagation in isotropic elastic three dimensional solid. *International Journal*
341 *of Fracture*, *179*(1-2), 45–57. doi: 10.1007/s10704-012-9771-6
- 342 Nejati, M., Paluszny, A., & Zimmerman, R. W. (2016). A finite element frame-
343 work for modeling internal frictional contact in three-dimensional fractured
344 media using unstructured tetrahedral meshes. *Computer Methods in Applied*
345 *Mechanics and Engineering*, *306*, 123–150. doi: 10.1016/j.cma.2016.03.028
- 346 Nikkhoo, M., & Walter, T. R. (2015). Triangular dislocation: an analytical, artefact-
347 free solution. *Geophysical Journal International*, *201*(2), 1119–1141.
- 348 Okada, Y. (1985). Surface deformation due to shear and tensile faults in a half-
349 space. *Bulletin of the seismological society of America*, *75*(4), 1135–1154.
- 350 Pinel, V., Carrara, A., Maccaferri, F., Rivalta, E., & Corbi, F. (2017). A two-step
351 model for dynamical dike propagation in two dimensions: Application to the
352 july 2001 etna eruption. *Journal of Geophysical Research: Solid Earth*, *122*(2),
353 1107–1125. doi: 10.1002/2016JB013630
- 354 Pollard, D. D., & Fletcher, R. C. (2005). *Fundamentals of structural geology*. Cam-
355 bridge University Press.
- 356 Pollard, D. D., & Townsend, M. R. (2018). Fluid-filled fractures in earth’s
357 lithosphere: Gravitational loading, interpenetration, and stable height
358 of dikes and veins. *Journal of Structural Geology*, *109*, 38–54. doi:
359 10.1016/j.jsg.2017.11.007
- 360 Reynolds, R. W., Geist, D., & Kurz, M. D. (1995). Physical volcanology and
361 structural development of sierra negra volcano, isabela island, galápagos
362 archipelago. *Geological Society of America Bulletin*, *107*(12), 1398–1410.
- 363 Rivalta, E., Corbi, F., Passarelli, L., Acocella, V., Davis, T., & Di Vito, M. A.
364 (2019). Stress inversions to forecast magma pathways and eruptive vent lo-
365 cation. *Science advances*, *5*(7), eaau9784.
- 366 Roman, A., & Jaupart, C. (2014). The impact of a volcanic edifice on intrusive and
367 eruptive activity. *Earth and Planetary Science Letters*, *408*, 1–8.
- 368 Rosen, P., Gurrola, E., Agram, P. S., Sacco, G. F., & Lavalle, M. (2015). The insar
369 scientific computing environment (isce): A python framework for earth science.
370 *AGUFM*, *2015*, IN11C–1789.
- 371 Salimzadeh, S., Zimmerman, R. W., & Khalili, N. (2020). Gravity hydraulic frac-
372 turing: A method to create self-driven fractures. *Geophysical Research Letters*,
373 e2020GL087563. doi: 10.1029/2020GL087563
- 374 Savage, W. Z., Powers, P. S., & Swolfs, H. S. (1984). *In situ geomechanics of*
375 *crystalline and sedimentary rocks; part v, rvt, a fortran program for an exact*
376 *elastic solution for tectonics and gravity stresses in isolated symmetric ridges*
377 *and valleys* (Tech. Rep.). Denver, Colorado: US Geological Survey.
- 378 Sigmundsson, F., Hooper, A., Hreinsdóttir, S., Vogfjörð, K. S., Ófeigsson, B. G.,
379 Heimisson, E. R., ... others (2015). Segmented lateral dyke growth in a rifting
380 event at bárdarbunga volcanic system, iceland. *Nature*, *517*(7533), 191–195.

- 381 Smittarello, D., Cayol, V., Pinel, V., Peltier, A., Froger, J.-L., & Ferrazzini, V.
 382 (2019). Magma propagation at piton de la fournaise from joint inversion of
 383 insar and gnss. *Journal of Geophysical Research: Solid Earth*, *124*(2), 1361–
 384 1387.
- 385 Sun, R. J. (1969). Theoretical size of hydraulically induced horizontal fractures
 386 and corresponding surface uplift in an idealized medium. *Journal of Geophysi-
 387 cal Research*, *74*(25), 5995–6011.
- 388 Tada, H., Paris, P., & Irwin, G. (2000). *The stress analysis of cracks handbook; third
 389 edition*. New York: ASME Press.
- 390 Thomas, A. L., & Pollard, D. D. (1993). The geometry of echelon fractures in rock:
 391 implications from laboratory and numerical experiments. *Journal of Structural
 392 Geology*, *15*(3-5), 323–334.
- 393 Vasconez, F. J., Ramón, P., Hernandez, S., Hidalgo, S., Bernard, B., Ruiz, M., ...
 394 Ruiz, G. (2018). The different characteristics of the recent eruptions of fer-
 395 nandina and sierra negra volcanoes (galápagos, ecuador). *Volcanica*, *1*(2),
 396 127–133.
- 397 Vigouroux, N., Williams-Jones, G., Chadwick, W., Geist, D., Ruiz, A., & Johnson,
 398 D. (2008). 4d gravity changes associated with the 2005 eruption of sierra negra
 399 volcano, galápagos. *Geophysics*, *73*(6), WA29–WA35.
- 400 Wessel, B., Huber, M., Wohlfart, C., Marschalk, U., Kosmann, D., & Roth, A.
 401 (2018). Accuracy assessment of the global tandem-x digital elevation model
 402 with gps data. *ISPRS Journal of Photogrammetry and Remote Sensing*, *139*,
 403 171–182.
- 404 Xu, W., & Jónsson, S. (2014). The 2007–8 volcanic eruption on jebel at tair island
 405 (red sea) observed by satellite radar and optical images. *Bulletin of Volcanol-
 406 ogy*, *76*(2), 795. doi: 10.1007/s00445-014-0795-9
- 407 Zia, H., & Lecampion, B. (2020). Pyfrac: A planar 3d hydraulic fracture simula-
 408 tor. *Computer Physics Communications*, *255*(107368), 1–11. doi: 10.1016/j.cpc
 409 .2020.107368